Sensitization of meningeal afferents to locomotion-related meningeal deformations in a migraine model

Andrew S Blaeser[1], Jun Zhao[1], Arthur U Sugden[2], Simone Carneiro-Nascimento[1], Mark L Andermann[2,3*], Dan Levy[1*]

[1] Department of Anesthesia, Critical Care and Pain Medicine, Beth Israel Deaconess Medical Center, Harvard Medical School, Boston, MA, 02215, USA
[2] Division of Endocrinology, Diabetes, and Metabolism, Department of Medicine, Beth Israel Deaconess Medical Center, Harvard Medical School, Boston, MA, 02215, USA
[3] Department of Neurobiology, Harvard Medical School, Boston, MA, 02115, USA

Corresponding Author: dlevy1@bidmc.harvard.edu

Correspondence may also be addressed to: manderma@bidmc.harvard.edu

ABSTRACT

Migraine headache is hypothesized to involve the activation and sensitization of trigeminal sensory afferents that innervate the cranial meninges. To better understand migraine pathophysiology and improve clinical translation, we used two-photon calcium imaging via a closed cranial window in awake mice to investigate changes in the responses of meningeal afferents using a preclinical model of migraine involving cortical spreading depolarization (CSD). A single CSD episode caused a seconds-long wave of calcium activation that propagated across afferents and along the length of individual afferents. Surprisingly, unlike previous studies in anesthetized animals with exposed meninges, only a very small afferent population was persistently activated in our awake mouse preparation, questioning the relevance of this neuronal response to the onset of migraine pain. In contrast, we identified a larger subset of meningeal afferents that developed augmented responses to acute three-dimensional meningeal deformations that occur in response to locomotion bouts. We observed increased responsiveness in a subset of afferents that were already somewhat sensitive to meningeal deformation before CSD. Furthermore, another subset of previously insensitive afferents also became sensitive to meningeal deformation following CSD. Our data provides new insights into the mechanisms underlying migraine, including the emergence of enhanced meningeal afferent calcium responses to movement-related meningeal deformations as a potential neural substrate underlying the worsening of migraine headache during physical activity.

INTRODUCTION

A large body of evidence supports the notion that migraine headache involves the trigeminal meningeal sensory system (Ashina et al., 2019; Levy and Moskowitz, 2023). Persistent discharge of meningeal afferents is thought to mediate the ongoing headache, while their augmented mechanosensitivity has been suggested to underlie migraine headache exacerbation during normally innocuous physical activities that cause transient intracranial hypertension, such as coughing and other types of straining (Blau and Dexter, 1981). Current understanding of migraine-related responses of meningeal afferents is largely based on animal models. For example, triggering an episode of cortical spreading depolarization (CSD), a self-propagating wave of neuronal and glial depolarizations thought to mediate migraine aura, causes persistent activation and mechanical sensitization of meningeal afferents (Zhao and Levy, 2015, 2016).

Despite the preclinical evidence implicating enhanced responsiveness of meningeal afferents as a driver of migraine headache (Olesen et al., 2009; Levy and Moskowitz, 2023), these studies have almost all used acute invasive experiments involving electrophysiological recordings in anesthetized animals with surgically exposed and mildly inflamed meninges (Levy et al., 2007). Moreover, studies documenting the mechanical sensitization of meningeal afferents were based on findings of increased responsiveness to artificial compressive forces applied to the dura of a depressurized brain. Hence, there is a significant gap in our understanding of whether and how meningeal afferents respond to migraine-related events under more naturalistic conditions in behaving animals with an intact and pressurized intracranial space.

To better understand migraine pathophysiology and improve clinical translation, we leveraged a newly developed approach for two-photon calcium imaging of meningeal afferent responses within the closed intracranial space of an awake-behaving mouse (Blaeser et al., 2022) in the CSD model of migraine. We imaged changes in afferent ongoing activity as well as afferent responses to three-dimensional meningeal deformation associated with locomotion following the triggering of a single CSD episode. Our data provides new insights into the mechanisms underlying migraine pathophysiology, including acute calcium signaling in meningeal afferent

fibers as a potentially critical nociceptive factor contributing to migraine pain and the emergence of enhanced meningeal afferent calcium responses to movement-related meningeal deformations as the neural substrate underlying the worsening of migraine headache during physical activity.

RESULTS

Propagating calcium activity across afferent fibers during CSD

To investigate meningeal afferent responses to CSD, we performed two-photon calcium imaging of GCaMP6s-expressing trigeminal afferent fibers innervating the meninges above the visual cortex (*n* = 325 fibers from 9 fields of view [FOV] from 7 mice, **Figure 1A**). We triggered a single CSD episode in the frontal cortex with a cortical pinprick. In every experiment, we detected a slow, CSD-like wave of calcium activity in numerous meningeal afferent fibers within one minute following the pinprick **(Figure 1B and Supplementary Movie S1)** as well as in background regions (likely reflecting signal from small, out-of-focus afferent branches). These calcium waves proceeded from the pinprick site in an anterior-to-posterior direction across the FOV **(Figure 1C)**. We also observed progressive activation of portions of individual afferent fibers aligned to the wave's movement direction. To characterize this phenomenon, we focused on sets of regions of interest (ROIs) belonging to the same long afferent fiber oriented along the direction of the calcium wave **(Figure 1D, Supplementary Movie 1)**. Compared to baseline afferent calcium signals observed during periods of locomotion, during which all ROIs belonging to an afferent were activated near-simultaneously, as reported previously (Blaeser et al., 2022), the sequential recruitment of ROIs along a fiber during the CSD-like wave was much slower **(Figure 1E-G)**. The proportion of afferents activated during this period exceeded the proportion activated during locomotion bouts **(Figure 1I)**. The magnitude of activation was also larger **(Figure 1J)**.

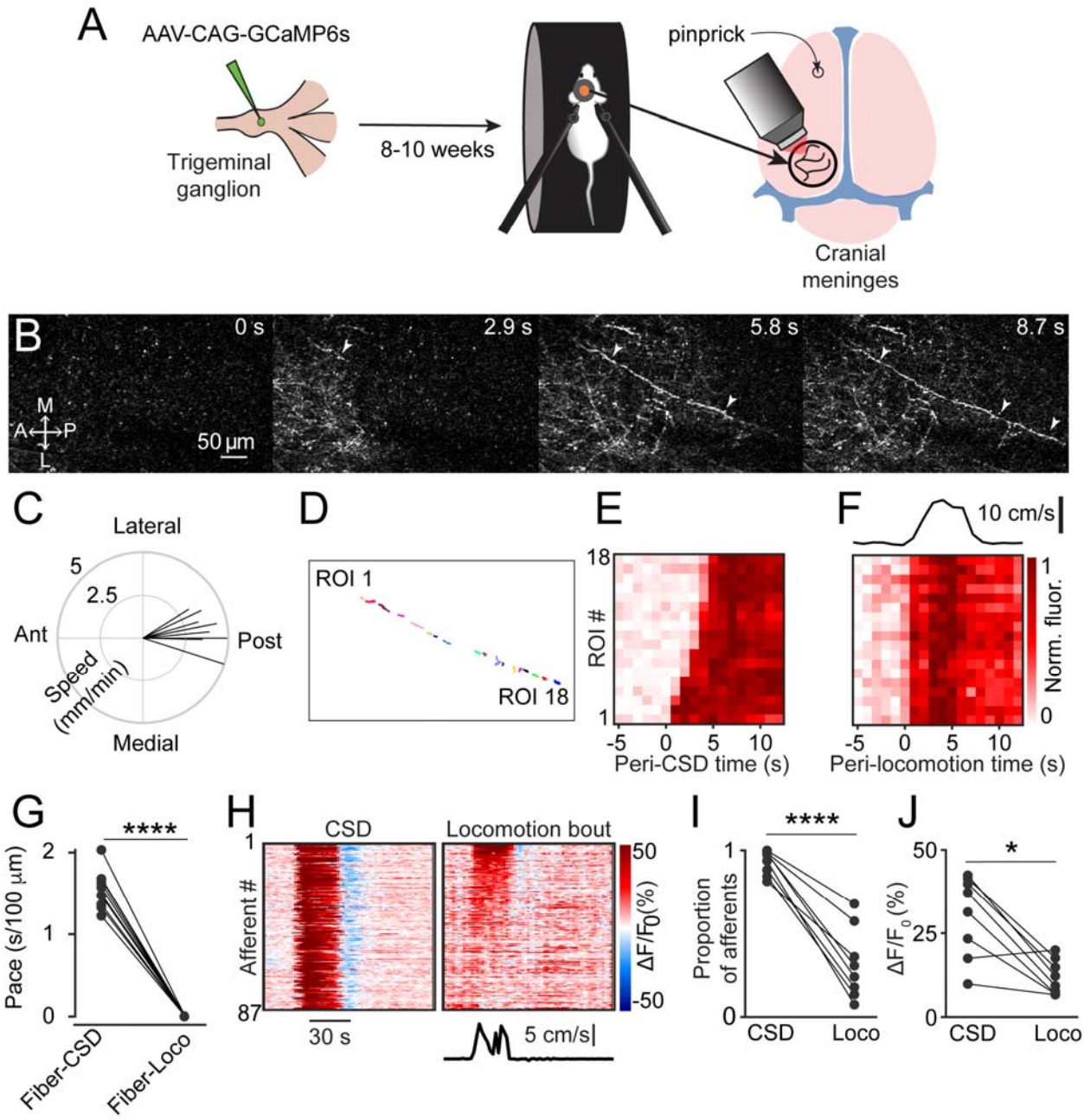

Figure 1. CSD drives wave-like calcium activity in meningeal afferents

(A) Mice received a trigeminal ganglion injection of an AAV to express GCaMP6s in trigeminal meningeal afferents. After 8-10 weeks, following the implantation of a headpost and a cranial window, mice were habituated to head restraint and subjected to two-photon calcium imaging while head-fixed on a running wheel to study the effect of pinprick-triggered CSD on the activity of meningeal afferents. **(B)** Example of a CSD-associated meningeal calcium wave that spreads across the field of view, with local segments of long afferent fibers becoming sequentially activated as the wave progresses (arrowheads). M: medial, L: lateral, A: anterior, P: posterior. **(C)** Summary of speed and direction of CSD-associated meningeal calcium waves, typically from anterior ('Ant.') (closer to where CSD was triggered anterior to

the cranial window) to more posterior locations ('Post.'). Speed estimates were obtained using the analysis method described in Figure S1A. On average, the wave progressed at 3.8±0.2 mm/min. **(D)** Map of 18 ROIs belonging to a single meningeal afferent fiber visible in B. **(E)** Activity heatmap of the afferent ROIs indicated in D illustrates progressive activation in response to CSD. **(F)** In contrast, the same afferent ROIs become activated simultaneously during a locomotion bout. **(G)** The pace of the CSD-associated afferent calcium wave was much slower than the spread of activity along the same afferent fibers during locomotion-evoked activity pre-CSD (**** $P < 0.0001$, paired, two-tailed t-test). **(H)** Example heatmaps of afferent activity observed during CSD showing different timecourse and magnitudes when compared to the activity observed during a locomotion bout. **(I)** Comparisons across all FOVs indicate a higher proportion of afferents exhibiting acute activation during the CSD vs. during locomotion (**** $P < 0.0001$, iterated bootstrap). **(J)** A higher proportion of afferents also displayed increased magnitudes of activation (* $P < 0.05$, paired, two-tailed t-test). See also Movie S1 and supplementary Fig. 1B.

A minority of afferents exhibit prolonged activation or suppression after CSD

In anesthetized rats with exposed meninges, CSD drives sustained increases in ongoing activity lasting tens of minutes in ~50% of meningeal afferents (Zhao and Levy, 2015). To directly assess CSD-related changes in afferent ongoing activity in awake mice with intact meninges, we focused on afferent responses during epochs of immobility between locomotion bouts. We observed low levels of ongoing activity at baseline before CSD (fluorescent events occurring 6.9±0.3% of the time), consistent with our previous study in naïve mice (Blaeser et al., 2022). Surprisingly, most afferents (~70%) did not display any change in ongoing activity following CSD. However, we identified sustained increases in ongoing activity in ~10% of the afferents. Surprisingly, we also observed a larger afferent population (~20%) whose activity was suppressed **(Figure 2A-C)**. Afferents with sustained activation showed increases in ongoing activity that emerged at a ~25 min delay on average **(Figure 2D)**. In contrast, afferents with sustained suppression showed decreases in ongoing activity beginning shortly after the passage of the acute calcium wave **(Figure 2D)**. The durations of the afferent activation or suppression were similar, lasting ~25 min on average **(Figure 2E)**.

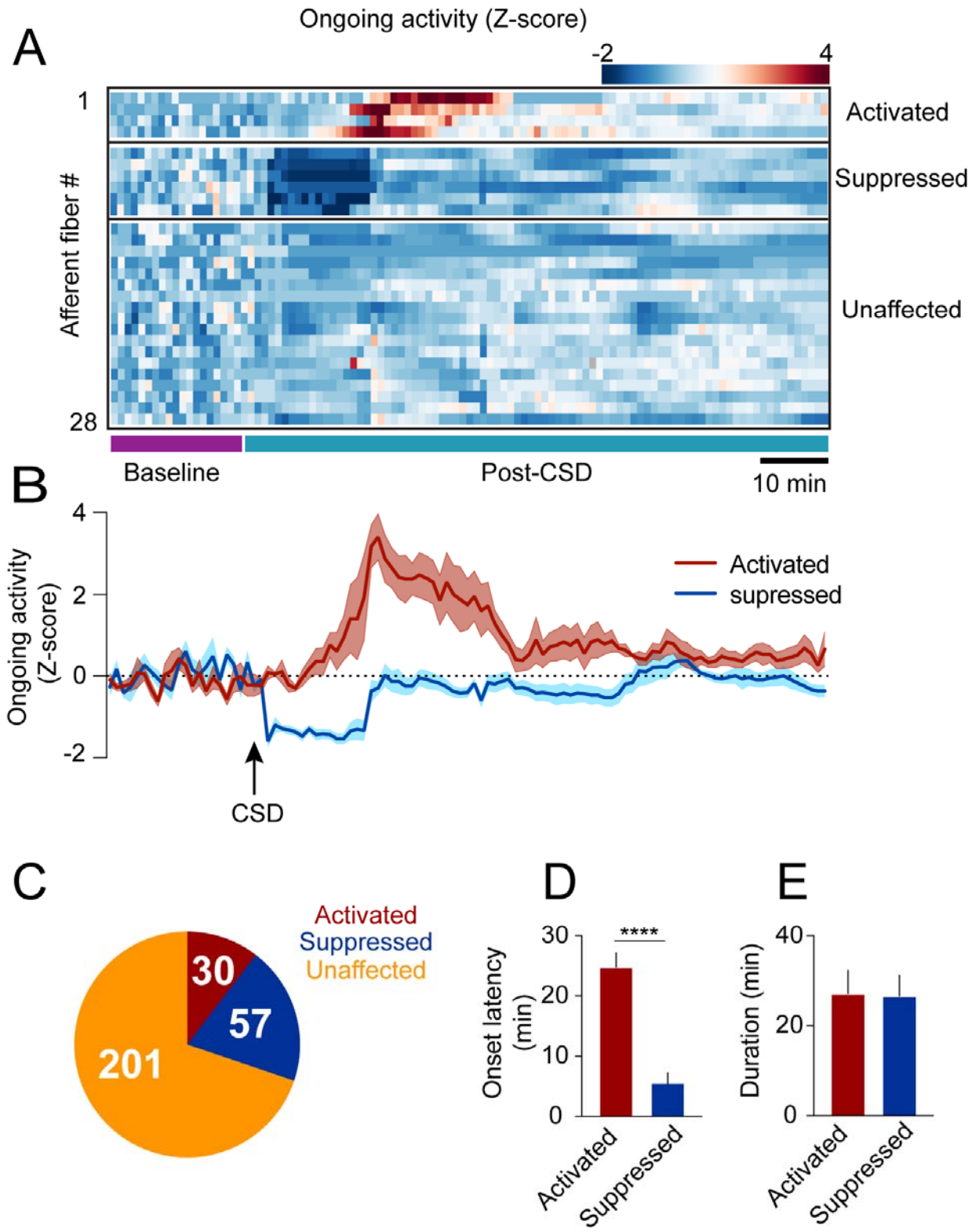
A
Ongoing activity (Z-score)
-2
4
1
28
Afferent fiber #
Activated
Suppressed
Unaffected
Baseline
Post-CSD
10 min
B
Ongoing activity (Z-score)
4
2
0
-2
Activated
supressed
CSD
C
Activated
Suppressed
Unaffected
30
57
201
D
Onset latency (min)
30
20
10
0
****
Activated
Suppressed
E
Duration (min)
40
20
0
Activated
Suppressed

Figure 2. CSD-related persistent changes in the ongoing activity of meningeal afferents

(A) Example heatmap of standardized ongoing activity (fraction of time afferents exhibited calcium events when the mouse is not locomoting) for all afferent fibers from a single FOV during baseline and up to 120 min following CSD. Data shows concatenated 1 min bins of activity. Afferents were either activated, suppressed, or unaffected by CSD. Note the delayed activation and immediate suppression in two small subsets of fibers. **(B)** Mean activity time course of the activated and suppressed afferents from the same population depicted in A. **(C)** Pie chart depicting the breakdown of the afferent subpopulations based on their change in ongoing activity following CSD. Most afferents were not affected (orange), while two smaller populations either exhibited prolonged activation (maroon) or suppression (blue) of ongoing activity following CSD (n=8 FOVs). **(D)** Afferents exhibiting prolonged activation had a longer onset latency than those exhibiting suppression (**** $P < 0.0001$, Mann Whitney t-test. Error bars: SEM). **(E)** The duration of increases in ongoing activity and suppressions in activity were similar ($P = 0.97$, two-tailed t-test. Error bars: SEM).

CSD augments afferent responsiveness associated with meningeal deformations

Locomotion drives acute meningeal deformations that can lead to the activation of mechanosensitive meningeal afferents (Blaeser et al., 2022). We wondered whether, following CSD, afferent responses to a given level of mechanical deformation would be enhanced (i.e., sensitization). If so, this could explain the exacerbation of migraine headache during physical activity. CSD suppresses cortical activity leading to decreased motor function (Houben et al., 2017). CSD also leads to neuronal swelling, vascular changes, and reduced extracellular space (Ayata and Lauritzen, 2015), which could affect meningeal deformations during locomotion and the associated afferent response. Hence, we first analyzed the effect of CSD on wheel running activity and the associated meningeal deformations. Mice spent less time locomoting after CSD than during the baseline period **(Figure 3B)**, and locomotion bout analysis revealed an overall reduction in bout rate following CSD **(Figure 3C)**. Remarkably, despite the overall reduction in locomotion following CSD, we observed similar bout characteristics at baseline and post-CSD, including bout duration **(Figure 3D)** and peak velocity **(Figure 3E)**. Given that CSD had minimal effect on locomotion bout characteristics, we next examined its effect on meningeal deformations. Surprisingly, CSD did not affect bout-related meningeal deformations: we observed similar scaling, shearing, and z-shift values **(Figure 3F-H)**.

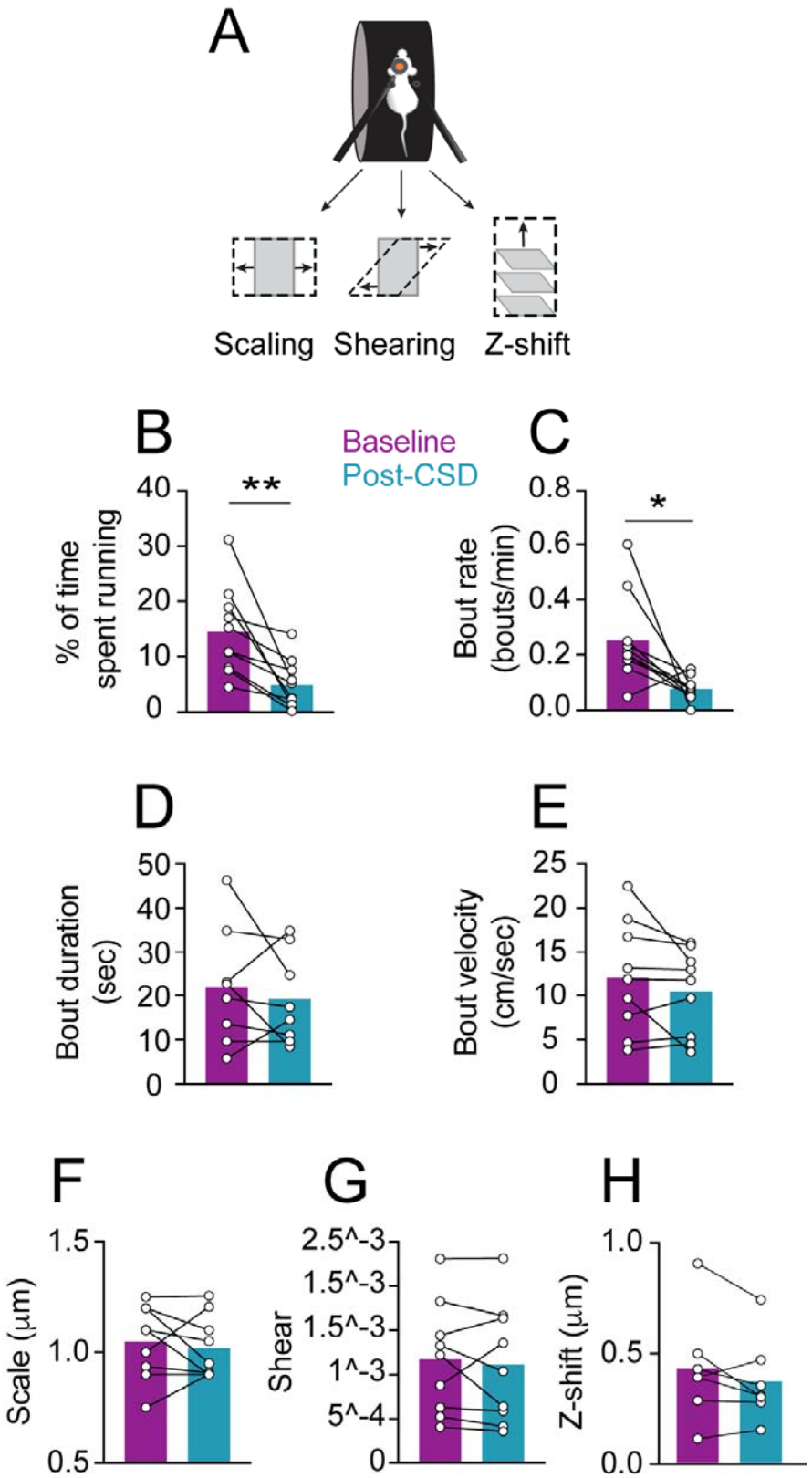
A
Scaling
Shearing
Z-shift
B
Baseline
Post-CSD
C
**
*
% of time spent running
Bout rate (bouts/min)
D
E
Bout duration (sec)
Bout velocity (cm/sec)
F
G
H
Scale (μm)
Shear
Z-shift (μm)

Figure 3. Locomotion and related meningeal deformations changes post CSD

(A) In head-fixed mice, wheel running drives meningeal scaling, shearing, and positive Z-shifts (i.e., meningeal movement toward the skull). **(B, C)** When compared to the baseline period, CSD was associated with an overall decrease in wheel running (** $P < 0.01$, paired t-test, $n = 9$) and locomotion bout rate (* $P < 0.05$, Wilcoxon, signed-rank test). **(D, E)** CSD, however, did not affect bout duration ($P = 0.50$, paired t-test) or bout peak velocity ($P = 0.18$, paired t-test). **(F, G, H)**. CSD also did not affect subsequent locomotion bout-evoked meningeal scaling, shearing, or Z-shift ($P = 0.56$; $P = 0.55$, $P = 0.18$, paired t-tests, respectively, $n = 9$ for scale and shear, n = 7 for Z-shift). Bars depict the mean.

Having shown that CSD does not affect meningeal deformations during locomotion, we next compared afferent responses during locomotion bouts before and after CSD. Initial observations of afferent activation during locomotion indicated enhanced responsiveness following CSD **(Figure 4A)**. To systematically investigate this augmented afferent response, we used general linear models (GLM; see (Blaeser et al., 2022) and Methods) to assess whether meningeal afferent activity becomes sensitized to the state of locomotion and/or to various aspects of meningeal deformation following CSD. We modeled each afferent's activity based on variables that describe (i) the binary state of locomotion, (ii) mouse velocity, and (iii) aspects of meningeal deformation, including scaling, shearing, and Z-shift. This model fit is shown for an example afferent in **Figure 4B**.

We first focused on afferents whose activity could be predicted by the same variables both at baseline and following CSD (i.e., afferents that exhibited sensitivities to locomotion and/or deformation signals both before and after CSD, $n = 67/325$ afferents, 9 FOV). Higher GLM coefficients for a given variable post-CSD indicate greater afferent response during an equal expression level of that variable. Thus, we defined an afferent as sensitized by CSD if its GLM coefficients post-CSD were larger than at baseline (i.e., stronger activation of afferents per unit deformation or locomotion; for example, see **Figure 4C**). Using these criteria, we identified elevated locomotion and/or deformation-related activity (i.e., sensitization) post-CSD in ~51% of afferents (n = 34; **Figure 4D**). In contrast, only 12% of afferents (n = 8) showed reduced locomotion- and deformation-related activity (i.e., desensitization) post-CSD. Sensitivity was unchanged in the remaining 37% of afferents (n = 25).

Meningeal afferent sensitization following CSD may reflect increased sensitivity to mechanical deformation and/or to other physiological processes that occur in response to locomotion

(Blaeser et al., 2022). Because locomotion and meningeal deformations are partially correlated (Blaeser et al., 2022), we next estimated their relative contributions to the augmented afferent responsiveness post-CSD by comparing, for each sensitized afferent, the GLM coefficients generated for baseline epochs and for post-CSD epochs. Surprisingly, we found that only the deformation coefficients were increased post-CSD **(Figure 4E)**, suggesting that meningeal afferent sensitization following CSD reflects primarily an increased sensitivity to mechanical deformation.

We next considered the possibility that sensitization is also manifested in the unmasking of responsiveness to locomotion and/or meningeal deformation in previously silent (i.e., insensitive) meningeal afferents (Levy and Moskowitz, 2023). Indeed, among the 245 afferents that were not well-fit before CSD, we detected a substantial population that developed a sensitivity to locomotion and deformation variables following CSD (n = 53, ~22%; i.e., whose activity could be well-predicted by locomotion and deformation variables following CSD). By contrast, far fewer neurons (n = 13) lost their sensitivity to these variables after CSD (i.e., afferents that were well fit before but not after CSD). Overall, the above finding show that four times more afferents displayed increased sensitivity than decreased sensitivity following CSD (87 vs. 21 afferents). This sensitized afferent population also displayed post-CSD increases in GLM coefficients related to deformation but not to locomotion **(Figure 4F)**.

To further quantify the importance of the locomotion and deformation variables to the afferent sensitization, we estimated their relative contributions to the overall ability of the models to predict the afferent activity pre- vs. post-CSD. To this end, we calculated the difference in model fit using the full model with all variables or models lacking either the set of deformation variables or locomotion variables. We found that the impact of deformation variables on the model fit was greater post-CSD than pre-CSD, while the impact of locomotion variables was similar pre- and post-CSD. This was true for afferents with models that were well fit both at baseline and following CSD **(Figure 4G**; purple subset in **Figure 4D)** and for those with models that were well fit only post-CSD **(Figure 4H**; magenta subset in **Figure 4D)**. Further analysis revealed that scale, shear, and Z-shift deformations were, on average, equally important in predicting the activity patterns of sensitized afferents **(Figure 4I)**. Taken together, these data

suggest that the afferent sensitization following CSD primarily involves increased afferent responsiveness to a mix of meningeal deformation variables rather than to locomotion-associated processes.

Previous studies in anesthetized rats suggested that the mechanisms underlying meningeal afferent mechanical sensitization are independent of those responsible for increased ongoing discharge in several migraine models, including CSD (Levy and Strassman, 2002; Zhang et al., 2011; Zhang et al., 2013; Zhao and Levy, 2018; Zhao et al., 2021). Here, using the CSD model in awake mice, we also found no association between sensitization and sustained changes in ongoing activity, as similar proportions of sensitized and non-sensitized afferents were activated, suppressed, or did not display any change in their ongoing activity following CSD **(Figure 4H)**.

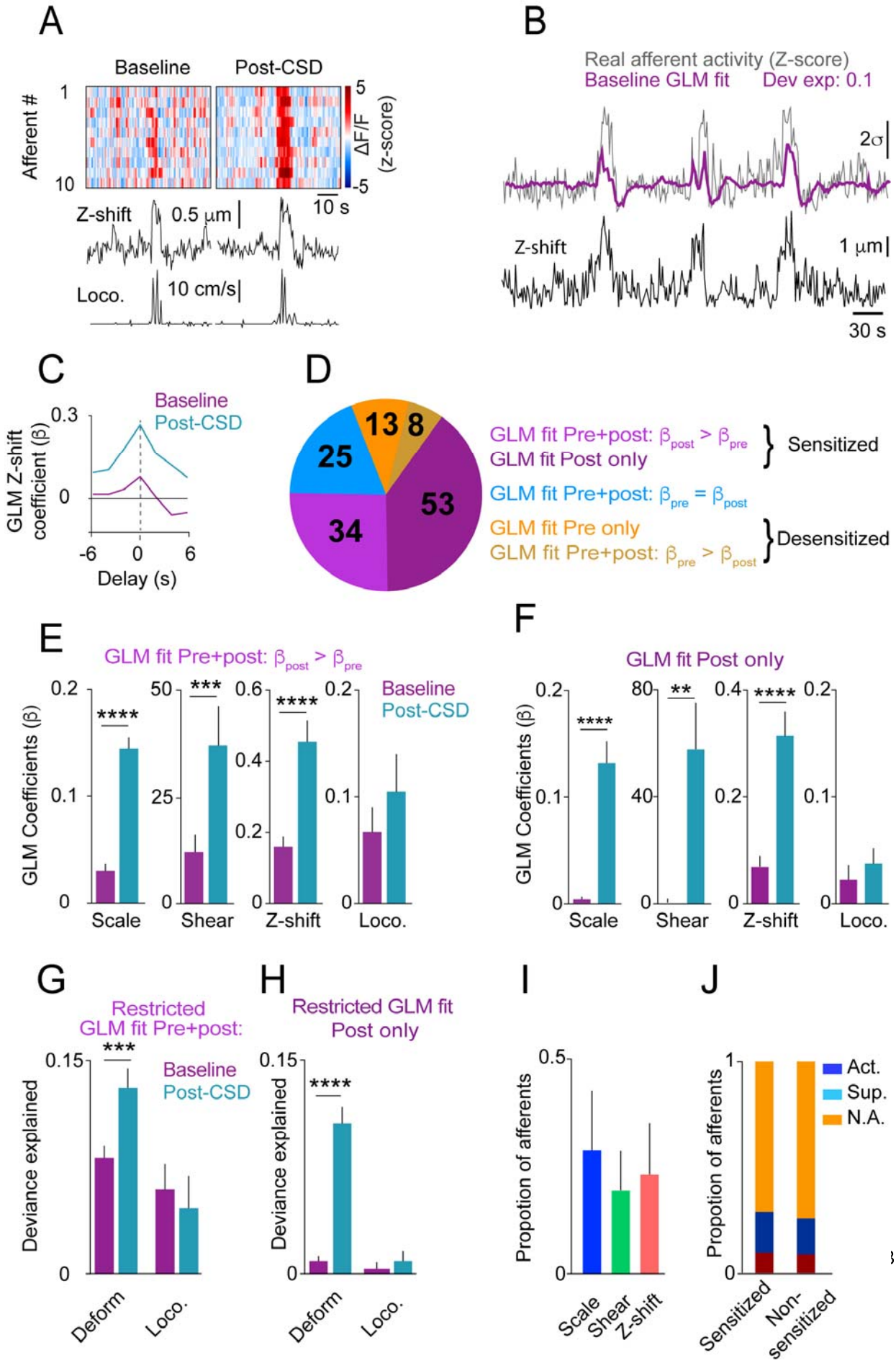
A
Baseline
Post-CSD
Afferent #
1
10
5
-5
ΔF/F
(z-score)
10 s
Z-shift
0.5 μm
Loco.
10 cm/s
B
Real afferent activity (Z-score)
Baseline GLM fit
Dev exp: 0.1
2σ
Z-shift
1 μm
30 s
C
Baseline
Post-CSD
GLM Z-shift coefficient (β)
0.3
0
-6
0
6
Delay (s)
D
13
8
25
53
34
GLM fit Pre+post: βpost > βpre
GLM fit Post only
Sensitized
GLM fit Pre+post: βpre = βpost
GLM fit Pre only
GLM fit Pre+post: βpre > βpost
Desensitized
E
GLM fit Pre+post: βpost > βpre
GLM Coefficients (β)
Baseline
Post-CSD
Scale
Shear
Z-shift
Loco.
F
GLM fit Post only
GLM Coefficients (β)
Scale
Shear
Z-shift
Loco.
G
Restricted
GLM fit Pre+post:
Deviance explained
Baseline
Post-CSD
Deform
Loco.
H
Restricted GLM fit
Post only
Deviance explained
Deform
Loco.
I
Propotion of afferents
Scale
Shear
Z-shift
J
Propotion of afferents
Act.
Sup.
N.A.
Sensitized
Non-sensitized

Figure 4. CSD leads to sensitization of meningeal afferents to local deformation signals

(A) Example of meningeal afferent sensitization following CSD. Locomotion and its related Z-shift (bottom traces) are comparable before (left) and after (right) CSD, but afferent fibers exhibit greater responses after CSD (heatmaps, top panels). **(B)** Example GLM fit of afferent activity before CSD. A raw calcium activity trace recorded pre-CSD (gray traces, z-scored; σ: 1 standard deviation) is plotted along with the model fit (purple). The deviance explained ('dev exp') is a metric of GLM fit quality and is above the threshold (0.05) for classifying an afferent's activity as reasonably well-fit by the GLM. **(C)** GLM β coefficients used as a metric of the coupling between the Z-shift and the activity of the example afferent shown in B across different delays. A maximal coefficient at zero delay indicates the alignment of activity with Z-shifts. Note the greater afferent activation per unit Z-shift after CSD relative to baseline, indicative of an augmented or sensitized response. **(D)** Pie chart indicating the numbers and distribution of all afferents that were well-fit by deformation and/or locomotion signals either before and/or after CSD. Afferents categorized as sensitized if they (i) had significant GLM fits both pre- and post-CSD, as well as higher coefficients for a given deformation and/or locomotion predictor post-CSD (purple) or (ii) were well-fit only post-CSD (magenta). Two small subsets of afferents categorized as desensitized had worse GLM fits post-CSD (mustard) or were no longer well-fit post-CSD (orange). The incidence of afferent sensitization exceeded that of desensitization ($P < 0.001$, χ^2 test). **(E, F)** Comparisons of pre- and post-CSD GLM coefficients for each of the deformation and locomotion predictors. Data are shown for sensitized afferents with well-fit models pre- and post-CSD (corresponding to the purple population in D) and for afferents with well-fit models only post-CSD (i.e., silent pre-CSD, corresponding to the magenta population in D). Mouse velocity coefficients were close to 0 in all cases and are not shown. In the two sensitized afferent populations, only coefficients related to deformation predictors increased post-CSD (** $p< 0.01$, *** $p< 0.001$, **** $p< 0.0001$, Wilcoxon sign rank test with correction for multiple analyses). **(G, H)** The response bias of sensitized afferents to meningeal deformation was further observed when comparing these GLMs to restricted GLMs that included only the group of deformation predictors or the group of locomotion predictors. The deviance explained by the deformation response component (estimated as the difference between the full GLM and the GLM lacking deformation variables) was significantly greater than for the locomotion response component in sensitized afferents that were well-fit pre- and post-CSD and for those that were well-fit only post-CSD (*** $P < 0.001$ and **** $P < 0.0001$, Wilcoxon test for G and H respectively). Bars depict mean; error bars indicate SEM. **(I)** Among the sensitized afferents with enhanced sensitivity to deformation variables, we observed a similar sensitization to scale, shear, and Z-shift variables. Bars depict mean; error bars indicate SEM. **(J)** There was no difference in the incidence of sensitized afferents among afferents that showed prolonged activation, prolonged suppression, or no change in ongoing activity post-CSD ($P = 0.9$, χ^2 test; cf. Figure 2).

DISCUSSION

Prior studies suggested that CSD drives meningeal nociception that can lead to the headache phase in migraine with aura. These studies, which mostly involved invasive experiments in anesthetized rats with surgically exposed meninges, showed prolonged activation and mechanical sensitization of meningeal afferents (Carneiro-Nascimento and Levy, 2022). To better understand migraine pathophysiology and improve clinical translation, we used two-photon calcium imaging to characterize, for the first time, CSD-related changes in the responsiveness of individual meningeal sensory afferents at the level of their peripheral nerve

fibers in the closed cranium of a behaving mouse. We show that a single CSD drives a wave of calcium activity across most afferents while producing a more prolonged change in ongoing activity in only a small subset. We then combined afferent calcium imaging with behavioral tracking of locomotion and estimates of local meningeal deformations. This approach revealed that CSD causes prolonged augmentation of afferent responsiveness to meningeal deformations associated with locomotion in previously sensitive afferents and emergent mechanical responses in previously silent afferents. These data support the notion that enhanced responsiveness of meningeal afferents to local meningeal deformation is the neural substrate for headache pain associated with physical activity following migraine onset.

The current study represents the first characterization of a CSD-associated calcium wave across meningeal afferent fibers and along the length of individual fibers. A rise in intracellular calcium detected by the GCaMP sensor normally indicates an action potential-evoked calcium influx (Chen et al., 2013). In contrast, the seconds-long wave of calcium elevation along individual afferent fibers is incongruent with the generation of action potentials. It may instead be related to subthreshold depolarizations (Li et al., 2022) and the opening of voltage-gated calcium channels (Awatramani et al., 2005). Our data thus support the notion that meningeal afferents can generate spatially localized and subthreshold yet powerful calcium transients during CSD. In turn, increased intracellular calcium could drive the release of sensory neuropeptides, such as CGRP, that can promote a local neurogenic inflammatory response linked to migraine pain (Akerman et al., 2003; Amrutkar et al., 2011; Levy and Moskowitz, 2023). The mechanism underlying the CSD-related afferent calcium wave could involve local depolarizing effects of diffusible excitatory molecules, such as potassium ions, whose cortical levels show a wave of elevation coincident with the propagation of the CSD wave (Suryavanshi et al., 2022). Since we also observed instantaneous elevation in calcium activity across subregions of individual afferent fibers oriented perpendicular to the calcium wave, we cannot exclude the possibility that some afferents also signal via action potentials during the passing of the CSD wave.

Electrophysiological recordings in anesthetized rats previously demonstrated prolonged elevations in spiking in ~50% of the somata of meningeal nociceptive afferents following CSD. In most recordings, increased activity emerged after a ~10 min delay and lasted almost an hour

following CSD (Zhao and Levy, 2015). In the awake mouse, the propensity and duration of these prolonged afferent responses were much smaller, bringing into question the relevance of this response to migraine pain. Surprisingly, a separate afferent population exhibited depression of afferent activity that began immediately after the acute response and also lasted for about 25 min. While species differences and the effects of anesthesia in the rat studies might play a role, meningeal irritation due to the acute craniotomy used in previous electrophysiological recording studies could be major contributing factor. Craniotomy may lead to increased meningeal permeability (Roth et al., 2014; Zhao et al., 2017), which could facilitate the transfer of algesic signals from the cortex. This process is likely less prevalent when using the chronic cranial window approach we employed in the current study, which has been shown to exhibit minimal inflammation (Goldey et al., 2014; Blaeser et al., 2022). An acute craniotomy also leads to a meningeal inflammatory response via the activation of local immune cells (Levy et al., 2007) and could prime meningeal afferents to develop prolonged activation following CSD. Such a priming mechanism, if occurs in susceptible individuals that suffer from migraines, could facilitate an increase in the activity of meningeal afferents and drive the headache during a migraine attack.

A major finding of this study is the post-CSD development of augmented meningeal afferent responsiveness meningeal deformations associated with locomotion bouts in awake mice with closed and pressurized meninges. Importantly, we previously found that the activity of most meningeal afferents around the time of locomotion is driven by mixed sensitivities to locomotion and to locomotion-related meningeal deformation signals (Blaeser et al., 2022). Here, we demonstrate that the amplification of afferent responsiveness following CSD relates primarily to enhanced neural gain in response to meningeal deformation rather than to other physiological processes associated with locomotion (e.g., vasodilation, intracranial pressure elevations) (Gao and Drew, 2016).

Meningeal afferents responding to physiological meningeal deformations may constitute a population of low-threshold mechanoreceptor (LTMR) afferents (von Buchholtz et al., 2020) whose activation under normal conditions is unlikely to produce headache. Our finding that CSD can augment the mechanical sensitivity of these afferents suggests that they may also possess nociceptive properties. This view is supported by the identification of a subpopulation of

cutaneous A-LTMR trigeminal afferents that also responds to noxious mechanical stimuli (von Buchholtz et al., 2021). Our data further suggest that about half of all afferents deemed to be sensitized following CSD are likely higher-threshold mechanosensitive afferents, as they were not driven by meningeal deformations or locomotion at baseline. Accordingly, local inflammation, which occurs following CSD, has been shown to recruit "silent" meningeal nociceptive afferents to become functional mechanonociceptors (Strassman and Levy, 2006). Overall, we propose that the sensitization of silent nociceptors, as well as of afferents with responsiveness to acute meningeal deformations at baseline, could produce a state of intracranial mechanical allodynia that underlies the exacerbation of migraine headaches during physical exertion and associated meningeal deformations.

MATERIALS AND METHODS

Animals

All experimental procedures complied with the ARRIVE and were approved by the Beth Israel Deaconess Medical Center Institutional Animal Care and Use Committee. All experiments were conducted on adult (8-16 weeks old) C57BL/6J mice (5 males, 2 females). Mice were group housed with standard mouse chow and water provided *ad libitum* before viral injection (see below). Mice used for *in vivo* two-photon imaging were singly housed and provided a running wheel, a hut, and a chew bar.

Surgical procedures and CSD induction

All surgical procedures were performed in anesthetized mice (isoflurane in O_2; 3.5% for induction, 1.5% for maintenance). Animals were given Meloxicam SR (4 mg/kg s.c.) for post-surgical analgesia. For monitoring calcium activity in meningeal afferents, 2.0 µl of AAV2/5.CAG.GCaMP6s.WPRE.SV40 (titer: $1X10^{13}$; Addgene) was injected into the left trigeminal ganglion (TG) using the following stereotaxic coordinates: 1.5 mm lateral and 0.3-0.8 mm anterior to Bregma and 7.0-7.2 mm ventral to the dura at a lateral-to-medial tilt with an angle of 22.5° relative to the dorsal-ventral axis. We previously verified this approach by examining GCaMP6s expression in TG somata and meningeal afferent fibers 8 weeks after

injection using immunohistochemistry (Blaeser et al., 2022). Mice used for *in vivo* two-photon imaging were instrumented with a titanium headpost and a 3 mm cranial window (Goldey et al., 2014; Blaeser et al., 2022) covering the posterior cortex (window centered roughly 1.5 mm lateral and 2 mm posterior to Bregma over the left hemisphere) 6-8 weeks after AAV injection. For CSD induction**,** a burr hole was drilled 1.5 mm anterior to the edge of the window until the brain's surface was barely visible. The burr hole was then plugged using silicone gel, and the mouse was allowed to recover. To trigger a single CSD episode, the silicone plug on the burr hole was removed, and a glass micropipette (50 μm diameter) was briefly inserted ~1 mm deep into the cortex for 2 seconds, as described previously (Zhao and Levy, 2016).

Wheel training

After at least one week of recovery following cranial window implantation, mice were head-fixed on a 3D-printed running wheel for gradual habituation (10 minutes to 1 hour over 3-4 days). The running wheel was mounted on a cantilever (Ramesh et al., 2018; Blaeser et al., 2022) to minimize downward forces on the bone and meninges produced while the mouse was pushing upwards against the headpost. Moreover, the strong cement used to bind all skull plates and headpost together (Goldey et al., 2014) further mitigated any movement-induced strain on the skull that might affect the underlying meninges. Mice displaying signs of stress were immediately removed from head fixation, and additional habituation days were added until mice tolerated head fixation without visible signs of stress. Mice received a high-calorie liquid meal replacement (Ensure) via a syringe as part of the habituation process.

Two-photon imaging

Calcium imaging was performed as recently described (Blaeser et al., 2022) while mice were head-fixed on the running wheel. We used a Nikon 16X, 0.8 NA water immersion objective on a resonant-scanning two-photon microscope (Neurolabware) and a MaiTai DeepSee laser, set to 920 nm with 25-40 mW power for GCaMP6s visualization. Digital zoom was set at 2.4X (626x423 μm^2 FOVs). In 7 experiments, we imaged a 60 mm volume (3D) using an electrically tunable lens (Optotune) at 1.03/s to capture afferents throughout the meninges. In two experiments, only single-plane (2D) data were collected at the cranial dura level at 15.5 Hz. In

every experiment, we conducted two imaging runs (30 min each) to collect baseline data, followed by four more 30 min runs post-CSD induction. In a subset of experiments in which the FOV included a visible large pial artery (n = 4), we verified the induction of a CSD by visualizing its vascular signature, including a brief vasoconstriction followed by dilation (Rosic et al., 2019) (Supplementary Fig. 1A).

Locomotion signals

Wheel position during each imaging run was recorded using an Arduino Uno board at 15.5 Hz. The instantaneous velocity was calculated as the time derivative of this signal and was downsampled to match the sampling rate of volume scans. Locomotion state was determined using a two-state Hidden Markov Model. Locomotion bouts were defined as periods when the locomotion state was sustained for at least two seconds (Blaeser et al., 2022).

Image processing and calcium signal extraction

All image processing and analyses were performed in MATLAB 2020a using custom software. Imaging movies were subjected to several preprocessing steps, including corrections for the lensing effect, rigid registration, z-interpolation, and affine registration (Blaeser et al., 2022). Registered 2D movies were analyzed using a PCA/ICA package (Mukamel et al., 2009) to extract masks of pixels with correlated activity. Users screened each prospective region of interest (ROI) for quality of morphology and fluorescence signal. ROIs with < 50 pixels were rejected. For each ROI included in subsequent analyses, we generated a dilated mask extending 8-21 pixels from the outer edge of the ROI, excluding any pixels that belonged to another ROI. This “neuropil” mask was used for the subtraction of background signals. In volumetric imaging, we generated a mean projection over all planes containing afferents for each volume. Then we ran the resulting 2D movie through the PCA/ICA procedure, yielding an initial set of 2D masks that represented putative 3D ROIs. An initial fluorescence trace extracted from each 2D mask was calculated by averaging fluorescence across all pixels in the mask. To identify which voxels in the original volumetric dataset contributed most strongly to each fluorescence trace, we calculated the Pearson correlation of this trace with the fluorescence timecourse of each voxel, resulting in a 3D volume of correlation values. These 3D correlation volumes were then screened

manually for quality of morphology and signal. The surviving volumes were thresholded at the 75th percentile of correlation across all voxels to form putative 3D ROI masks.

Fluorescence signals

We calculated raw fluorescence signals at each time point for the ith ROI (F^i_{ROI}) and its corresponding neuropil mask (F^i_{np}), as the simple arithmetic means of all pixels/voxels within each ROI mask. Next, we calculated $F^i = F^i_{ROI} - F^i_{np} + \langle F^i_{np} \rangle$, where brackets denote the mean across the entire recording. We then calculated the corresponding baseline signal F^i_0 as the 10th percentile of a moving window for the last 32 seconds (Sugden et al., 2020). We then calculated the normalized, baseline-subtracted time series $\Delta F/F_0 = (F^i - F^i_0)/ F^i_0$. This signal was standardized akin to a Z-score operation by subtracting the median value and dividing by the standard deviation (calculated during quiet wakefulness, an epoch with low levels of evoked activity). Fluorescence events were defined as periods where the signal consistently exceeded a value of 1 for at least one second and where peak fractional change in fluorescence ($\Delta F/F_0$) was at least 5%.

Identifying calcium activity in afferent fibers

To analyze calcium activity related to an afferent fiber, sets of ROIs putatively belonging to the same axon were initially identified using a previously described method (Liang et al., 2018; Blaeser et al., 2022). Briefly, we calculated the pairwise fluorescence event correlation between ROIs during quiet wakefulness, thresholding at 0.7 correlation. We then calculated the cosine dissimilarity between the full set of correlation coefficients for each pair of ROIs, which in turn was used to calculate the linkage between each pair. Finally, hierarchical clustering was performed using a cutoff value of 2. This procedure generated sets of ROIs that were mutually highly correlated. We then visually inspected each cluster and manually identified the subsets of ROIs that unambiguously covered the same specific afferent fiber without any branching. We used the mean activity of these ROI subsets to analyze each afferent's calcium activity.

CSD-associated calcium wave characterization

To detect the CSD-associated meningeal calcium wave (see Supplementary Fig. 1B), we first calculated the mean fluorescence signal over all voxels in the FOV, $F_{FOV}(t)$, and its time derivative dF_{FOV}/dt, in the first 5 minutes after cortical pinprick. To identify the timing of the CSD, we first defined an initial period, t_{inital}, between the derivative's maximum and minimum. We then calculated baseline fluorescence, F_{pre}, as the 10th percentile value of F_{FOV} in the 30 sec before the initial period and a normalized fluorescence signal, $\Delta F/F_{pre} = (F_{FOV} - F_{pre})/F_{pre}$. Next, we defined a threshold value as $0.1*\max(\Delta F(t_{initial})/F_{pre})$. The wave's final onset and offset times were defined as the points around the peak where $\Delta F_{FOV}/F_{pre}$ crossed the threshold value.

To measure the propagation of the calcium wave throughout the meninges, we estimated the wave's onset time at different X and Y positions within the FOV. Briefly, we gathered all the data from the peri-CSD wave from -6 to 14 s relative to the calcium wave onset time determined above. All voxels belonging to or neighboring (within 8 pixels) ROIs were excluded to focus on the overall wavelike advancement in the background 'neuropil' fluorescence signal (which integrates background fluorescence across depths and thus reflects a smooth estimate of mean activity in a given region). The resulting series of images was then divided into 40x40 pixel spatial bins, and mean fluorescence signals $F_{np}^{bin}(t)$ were calculated. The time of estimated onset of the CSD-associated wave at a given bin was estimated by fitting $F_{np}^{bin}(t)$ to a logistic function, $A/(1+\exp(-(t-t_{onset})/\tau)) + K$. Fits with $R^2 < 0.5$, or $\tau > 2$ s, or $\tau < 0$ s, were excluded. The wave's speed was estimated by linear regression of onset times as a function of distance. The direction of the wave was determined by estimating the contour of the wavefront at the median bin onset time, fitting this contour to a line, and then calculating the vector orthogonal to that line.

To specifically examine the propagation of the fluorescence signals along long (>200 mm) individual afferent fibers, we determined the timing of CSD-associated wave onset by fitting each ROI's peri-wave fluorescence signals to a sigmoidal function and then estimating the speed of propagation by linear regression of onset times as a function of distance. For comparison, this procedure was repeated using the peri-locomotion bout signals. Since locomotion-associated activation occurred essentially simultaneously (i.e., $\Delta t = 0$ s), even for distant ROIs, we report these results in terms of the pace (the inverse of speed) to avoid dividing by zero.

Assessment of CSD-evoked changes in afferent ongoing activity

To determine changes in ongoing afferent activity, we focused on the periods of immobility between locomotion bouts (stillness). We minimized any residual effects of locomotion-related activity by excluding 30-sec epochs prior to and following the locomotion bouts. We then analyzed fluorescence events as above. We estimated levels of ongoing activity rate from the normalized Z-score timecourses as the fraction of time the afferents exhibited fluorescent events (defined as above) during each one-minute interval. We defined afferents with post-CSD increases or suppression of activity if changes in ongoing activity lasted >10 consecutive min and began within 30 min post the CSD wave (Zhao et al., 2021).

Meningeal deformation signals

Estimates of meningeal translation, scaling, and shearing were extracted from the affine transformation matrices used for image alignment, as described previously (Blaeser et al., 2022). Corrections made for small motions along the z-axis (Shipley et al., 2020) provided a measure of how much each plane moved up or down relative to a reference volume ("Z-shift"), scaling, and Z-shifts were converted from pixels to microns. Positive Z-shifts indicate meningeal movement toward the skull.

General linear models

To classify afferent responses, we fit Gaussian general linear models (GLM) for locomotion, deformation, and fluorescence using the glmnet package in Matlab. To allow for the possibility of a delay between the predictor and response, we expanded the set of predictors to include variables at varying delays relative to calcium activity (Driscoll et al., 2017; Ramesh et al., 2018; Blaeser et al., 2022). Specifically, for each variable, we generated a set of temporally shifted versions spanning a time window from -6 s to +6 s. These sets of arrays of temporal shifts for each variable were joined to form an array of temporally shifted predictor signals. The GLM was fit on 75% of the data for each cell with elastic net regularization (α= 0.01). We then used the GLM coefficients to measure the deviance explained on the remaining 25% of the data. The relative explanatory value of locomotion or deformation variables was calculated by refitting the GLM after excluding the family of predictors (locomotion state and velocity for evaluating the effect of locomotion and scale, shear, and Z-shift for examining the effect of deformation) and

calculating the difference in deviance explained by the full model versus the model lacking a given family of predictor variables. All GLM models underwent 10-fold cross-validation.

Data analysis and statistics

Data analyses were performed in MATLAB 2020a and Prism 9. Sample sizes were not predetermined by power analysis but are similar to previous studies (Sugden et al., 2020; Blaeser et al., 2022). Two-tailed paired *t*-tests and one-way analysis of variance (ANOVA) followed by a post-hoc Tukey test were used for all parametric data. Data with non-Gaussian distributions were analyzed using a Wilcoxon matched-pairs signed rank sum test or a Mann-Whitney test. Corrections for multiple comparisons were adjusted using the False Discovery Rate approach. Bootstrapped confidence intervals and hypothesis tests were generated using the 'iboot' iterated bootstrapping package (Penn, 2020). Data are presented as averages ± standard error of the mean (SEM) unless otherwise noted. *P*-values are indicated as follows: $P < 0.05$ (*), $P < 0.01$ (**), $P < 0.001$ (***), $P < 0.0001$ (****).

Data availability

The code used to analyze locomotion data is available at: https://github.com/ablaeser/LocomotionAnalysis. Code for organizing and processing two-photon imaging data is available at: https://github.com/ablaeser/MovieProcessing. The code for analysis of calcium imaging is available at: https://github.com/ablaeser/CalciumAnalysis. Any additional information required to reanalyze the data reported in this paper is available from the lead contact upon request.

REFERENCES

Akerman S, Williamson DJ, Goadsby PJ (2003) Voltage-dependent calcium channels are involved in neurogenic dural vasodilatation via a presynaptic transmitter release mechanism. Br J Pharmacol 140:558-566.

Amrutkar DV, Ploug KB, Olesen J, Jansen-Olesen I (2011) Role for voltage gated calcium channels in calcitonin gene-related peptide release in the rat trigeminovascular system. Neuroscience 172:510-517.

Ashina M, Hansen JM, Do TP, Melo-Carrillo A, Burstein R, Moskowitz MA (2019) Migraine and the trigeminovascular system-40 years and counting. Lancet Neurol 18:795-804.

Awatramani GB, Price GD, Trussell LO (2005) Modulation of transmitter release by presynaptic resting potential and background calcium levels. Neuron 48:109-121.

Ayata C, Lauritzen M (2015) Spreading Depression, Spreading Depolarizations, and the Cerebral Vasculature. Physiol Rev 95:953-993.

Blaeser AS, Sugden AU, Zhao J, Carneiro-Nascimento S, Shipley FB, Carrie H, Andermann ML, Levy D (2022) Trigeminal afferents sense locomotion-related meningeal deformations. Cell Rep 41:111648.

Blau JN, Dexter SL (1981) The site of pain origin during migraine attacks. Cephalalgia 1:143-147.

Carneiro-Nascimento S, Levy D (2022) Cortical spreading depression and meningeal nociception. Neurobiol Pain 11:100091.

Chen TW, Wardill TJ, Sun Y, Pulver SR, Renninger SL, Baohan A, Schreiter ER, Kerr RA, Orger MB, Jayaraman V, Looger LL, Svoboda K, Kim DS (2013) Ultrasensitive fluorescent proteins for imaging neuronal activity. Nature 499:295-300.

Driscoll LN, Pettit NL, Minderer M, Chettih SN, Harvey CD (2017) Dynamic Reorganization of Neuronal Activity Patterns in Parietal Cortex. Cell 170:986-999 e916.

Gao YR, Drew PJ (2016) Effects of Voluntary Locomotion and Calcitonin Gene-Related Peptide on the Dynamics of Single Dural Vessels in Awake Mice. J Neurosci 36:2503-2516.

Goldey GJ, Roumis DK, Glickfeld LL, Kerlin AM, Reid RC, Bonin V, Schafer DP, Andermann ML (2014) Removable cranial windows for long-term imaging in awake mice. Nature protocols 9:2515-2538.

Houben T, Loonen IC, Baca SM, Schenke M, Meijer JH, Ferrari MD, Terwindt GM, Voskuyl RA, Charles A, Van Den Maagdenberg AM, Tolner EA (2017) Optogenetic induction of cortical spreading depression in anesthetized and freely behaving mice. Journal of Cerebral Blood Flow & Metabolism 37:1641-1655.

Levy D, Strassman AM (2002) Distinct sensitizing effects of the cAMP-PKA second messenger cascade on rat dural mechanonociceptors. J Physiol 538:483-493.

Levy D, Moskowitz MA (2023) Meningeal Mechanisms and the Migraine Connection. Annual review of neuroscience.

Levy D, Burstein R, Kainz V, Jakubowski M, Strassman AM (2007) Mast cell degranulation activates a pain pathway underlying migraine headache. Pain 130:166-176.

Li Z, Boesmans W, Kazwiny Y, Hao MM, Vanden Berghe P (2022) Simultaneous whole-cell patch-clamp and calcium imaging on myenteric neurons. Am J Physiol Gastrointest Liver Physiol 323:G341-G347.

Liang L, Fratzl A, Goldey G, Ramesh RN, Sugden AU, Morgan JL, Chen C, Andermann ML (2018) A Fine-Scale Functional Logic to Convergence from Retina to Thalamus. Cell 173:1343-1355 e1324.

Mukamel EA, Nimmerjahn A, Schnitzer MJ (2009) Automated analysis of cellular signals from large-scale calcium imaging data. Neuron 63:747-760.

Olesen J, Burstein R, Ashina M, Tfelt-Hansen P (2009) Origin of pain in migraine: evidence for peripheral sensitisation. Lancet Neurol 8:679-690.

Penn AC (2020) iboot: Iterated bootstrap for small samples or samples with complex dependence structures In, pp This package of functions can be used to estimate uncertainty (confidence intervals) and test hypotheses (p-values) using bootstrap. Variations of the bootstrap are included that improve the accuracy of bootstrap statistics for small samples

and samples with complex dependence structures. The Octave statistics-bootstrap package is forked from the GitHub repository iboot. https://github.com/acp29/iboot.
Ramesh RN, Burgess CR, Sugden AU, Gyetvan M, Andermann ML (2018) Intermingled Ensembles in Visual Association Cortex Encode Stimulus Identity or Predicted Outcome. Neuron 100:900-915 e909.
Rosic B, Dukefoss DB, Abjorsbraten KS, Tang W, Jensen V, Ottersen OP, Enger R, Nagelhus EA (2019) Aquaporin-4-independent volume dynamics of astroglial endfeet during cortical spreading depression. Glia 67:1113-1121.
Roth TL, Nayak D, Atanasijevic T, Koretsky AP, Latour LL, McGavern DB (2014) Transcranial amelioration of inflammation and cell death after brain injury. Nature 505:223-228.
Shipley FB et al. (2020) Tracking Calcium Dynamics and Immune Surveillance at the Choroid Plexus Blood-Cerebrospinal Fluid Interface. Neuron 108:623-639 e610.
Strassman AM, Levy D (2006) Response properties of dural nociceptors in relation to headache. J Neurophysiol 95:1298-1306.
Sugden AU, Zaremba JD, Sugden LA, McGuire KL, Lutas A, Ramesh RN, Alturkistani O, Lensjo KK, Burgess CR, Andermann ML (2020) Cortical reactivations of recent sensory experiences predict bidirectional network changes during learning. Nat Neurosci 23:981-991.
Suryavanshi P, Reinhart KM, Shuttleworth CW, Brennan KC (2022) Action Potentials Are Critical for the Propagation of Focally Elicited Spreading Depolarizations. J Neurosci 42:2371-2383.
von Buchholtz LJ, Lam RM, Emrick JJ, Chesler AT, Ryba NJP (2020) Assigning transcriptomic class in the trigeminal ganglion using multiplex in situ hybridization and machine learning. Pain 161:2212-2224.
von Buchholtz LJ, Ghitani N, Lam RM, Licholai JA, Chesler AT, Ryba NJP (2021) Decoding Cellular Mechanisms for Mechanosensory Discrimination. Neuron 109:285-298 e285.
Zhang X, Kainz V, Zhao J, Strassman AM, Levy D (2013) Vascular extracellular signal-regulated kinase mediates migraine-related sensitization of meningeal nociceptors. Ann Neurol 73:741-750.
Zhang XC, Kainz V, Burstein R, Levy D (2011) Tumor necrosis factor-alpha induces sensitization of meningeal nociceptors mediated via local COX and p38 MAP kinase actions. Pain 152:140-149.
Zhao J, Levy D (2015) Modulation of intracranial meningeal nociceptor activity by cortical spreading depression: a reassessment. J Neurophysiol 113:2778-2785.
Zhao J, Levy D (2016) Cortical Spreading Depression Promotes Persistent Mechanical Sensitization of Intracranial Meningeal Afferents: Implications for the Intracranial Mechanosensitivity of Migraine. eNeuro 3:ENEURO.0287-0216.2016.
Zhao J, Levy D (2018) Dissociation between CSD-Evoked Metabolic Perturbations and Meningeal Afferent Activation and Sensitization: Implications for Mechanisms of Migraine Headache Onset. J Neurosci 38:5053-5066.
Zhao J, Blaeser AS, Levy D (2021) Astrocytes mediate migraine-related intracranial meningeal mechanical hypersensitivity. Pain 162:2386-2396.
Zhao J, Bree D, Harrington MG, Strassman AM, Levy D (2017) Cranial dural permeability of inflammatory nociceptive mediators: Potential implications for animal models of migraine. Cephalalgia 37:1017-1025.

ACKNOWLEDGMENTS

We thank members of the Andermann and Levy labs for helpful discussions, and Fred Shipley, Glenn Goldey, Kiersten M. Levandowski, Helaine Gariepy, Andrew Lutas, and Osama Alturkistani for advice and technical assistance. We thank Drs. Jayaraman, Kerr, Kim, Looger, and Svoboda and the GENIE Project, Janelia Farm Research Campus, HHMI, for GCaMP6.

FUNDING

Support was provided by NIH DP2DK105570, R01DK109930, DP1AT010971, the Pew Innovation Fund (to M.L.A.); 5R21NS101405 (to D.L and M.L.A.); R01NS086830; R01NS078263; R01NS115972 (to D.L.); and T32 5T32DK007516 (A.U.S.).

SUPPLEMENTAL MATERIAL

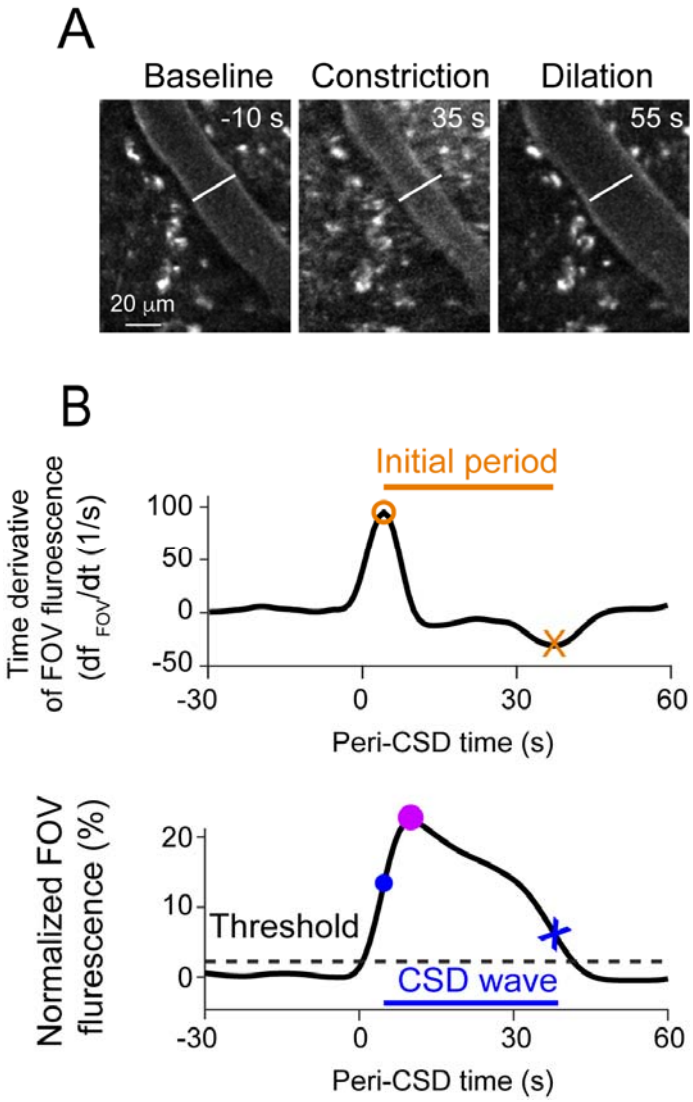

Figure S1. Further analyses of hemodynamics and calcium activity related to the CSD wave

(A) Example cropped subregion of a field-of-view (FOV) demonstrating a typical pial vascular response to CSD, including an initial constriction (middle) followed by dilation (right). (**B)** Analysis used for detecting the CSD-associated meningeal calcium wave. Top: Time derivative of the FOV-averaged fluorescence signal over the first 90 s of imaging after the cortical pinprick. An initial period was defined between the derivative's maximum (orange circle) and minimum (orange X) and was used to define the baseline fluorescence value (F_{pre}). Bottom: Normalized FOV fluorescence signal. The maximum within the initial period (purple circle) is taken as the peak of the CSD-associated wave, and a threshold value

(dashed line) is defined as 10% of that peak value. The threshold crossings before (blue circle) and after (blue x) the peak define the wave's onset and offset, respectively.

Movie S1. CSD-associated afferent calcium wave. Related to Figure 1 and Supplemental Fig 1. Movies of the CSD-associated calcium waves spread from anterior to posterior, as shown for two example waves from different mice. Note the spread of calcium activation along individual afferents in each movie. Scale bars: 50 µm.